

Modeling Dynamic Neural Activity by combining Naturalistic Video Stimuli and Stimulus-independent Latent Factors

Finn Schmidt¹ Polina Turishcheva¹ Suhas Shrinivasan¹ Fabian H. Sinz^{1,2}

Abstract

Understanding how visual processing of natural stimuli and internal brain states interact in populations of neurons remains an open question in neuroscience. Currently there are no dynamic encoding models that explicitly model a latent state and the entire neuronal response distribution. We address this gap by proposing a probabilistic model that predicts the joint distribution of the neuronal responses from video stimuli and stimulus-independent latent factors. After training and testing our model on mouse V1 neuronal responses, we find that it outperforms video-only models in terms of log-likelihood and achieves improvements in likelihood and correlation when conditioned on responses from other neurons. Furthermore, we find that the learned latent factors strongly correlate with mouse behavior and that they exhibit patterns related to the neurons' position on visual cortex, although the model was trained without behavior and cortical coordinates. Our findings demonstrate that unsupervised learning of latent factors from population responses can reveal biologically meaningful structure that bridges sensory processing and behavior, without requiring explicit behavioral annotations during training. Code will be available upon publication.

1. Introduction

Predicting the activity of sensory neurons is a major goal of computational neuroscience towards understanding the mechanisms of information encoding in the brain. In particular, accurately predicting neural responses in the primary visual cortex (V1) in response to a given stimulus could

¹Department of Computer Science and Campus Institute Data Science, University of Göttingen, Göttingen, Germany
²Department of Neuroscience, Center for Neuroscience and Artificial Intelligence, Baylor College of Medicine, Houston, Texas, USA. Correspondence to: Finn Schmidt <finn.schmidt@uni-goettingen.de>, Fabian H. Sinz <sinz@uni-goettingen.de>.

Preliminary work. Under review by the International Conference on Machine Learning (ICML). Do not distribute.

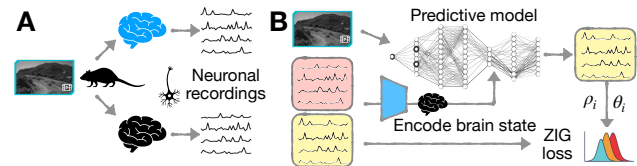


Figure 1. **A.** Problem statement: an animal is watching the same video but different brain states lead to different neuronal responses. **B.** Proposed solution: Infer the brain state via a probabilistic latent variable model that predicts marginal Zero-Inflated-Gamma (ZIG) distributions for each neuron.

provide deep insights into how the brain processes visual information. However, this task remains challenging because neural activity in the visual cortex exhibits variability not only across different visual stimuli but also across repeated presentations of the same stimulus (Tomko & Crapper, 1974; Shadlen & Newsome, 1998). This variability arises from the influence of numerous unobservable factors that the visual cortex integrates into its processing. For example, the activity in the visual cortex is influenced by factors such as behavioral tasks (Cohen & Newsome, 2008; Haefner et al., 2016), attention (Mitchell et al., 2009; Cohen & Maunsell, 2009; Briggs et al., 2013), and general brain states correlated with behavior (Niell & Stryker, 2010; Ecker et al., 2014; Stringer et al., 2019; Reimer et al., 2014). This stimulus-conditioned variability, driven by these additional factors, leads to strong and complex correlations among neurons. Those correlations are usually referred to as noise correlations (Tolhurst et al., 1983). Thus, understanding the sensory processing of the visual cortex requires models that capture both stimulus-dependent and shared stimulus-conditioned variability (Bashiri et al., 2021). One approach is to represent those internal fluctuations as latent variable models, that describe the distribution of neuronal activity to a given stimulus in terms of a latent state shared across neurons. To this end, such models require a probabilistic framework to effectively incorporate and infer these latent variables.

The majority of video encoding models for neuronal activity in visual cortex focuses on models that predict neural activity conditioned solely on the stimulus (Sinz et al., 2018; Turishcheva et al., 2023; Wang et al., 2023a) or on mapping neural activity to meaningful low-dimensional latent

spaces, independent or only conditioning on the underlying task or stimulus (Jensen et al., 2021; Sussillo et al., 2016; Gokcen et al., 2022; Schneider et al., 2023). To the best of our knowledge, only few models exist that capture the correlated variability of large neuronal populations and the visual stimuli as input (Bashiri et al., 2021). None of them are designed for dynamic video-based stimuli. In the current paper, we address this gap with the following contributions:

- We propose a video based encoding model for mouse primary visual cortex (V1) that models the distribution of neuronal activity in terms of video inputs and latent shared activity via a latent space (Figure 1).
- We show that the model’s latent variables are meaningful, as they are strongly correlating with mouse behavior despite no exposure to behavioral data (like in Bashiri et al., 2021; Niell & Stryker, 2010; Reimer et al., 2014; Stringer et al., 2019).
- Our model surpasses comparable models without latent in predicting neuron responses in log-likelihood.
- Our model outperforms other models in terms of predictive performance when conditioning the predicted response on other parts of the neuronal population.
- We find that the learned latent factors exhibit topographic patterns along the cortical surface although the model was never exposed to cortical position data.

2. Related works

Existing data-driven neural response prediction methods fall into three categories:

1. deterministic models that predict neural activity from visual stimuli but do not account for response uncertainty and variability (Sinz et al., 2018; Höfling et al., 2022; Wang et al., 2023a; Turishcheva et al., 2023; Vystřilová et al., 2024)
2. probabilistic models focused on deriving a latent state from neural responses, sometimes conditioning on the external sensory inputs (Gokcen et al., 2022; Sussillo et al., 2016; Yu et al., 2009; Schneider et al., 2023)
3. and models, using both sensory input and neuronal activity to predict the activity of other neurons (Bashiri et al., 2021; Kim et al., 2023).

Appendix A summarizes related works in terms of inputs, outputs and presence of latents.

Deterministic models for visual cortex. Recent advances in deep learning, particularly convolutional neural networks (CNNs) trained on image recognition tasks (Yamins et al., 2014; Cadieu et al., 2014; Cadena et al., 2019a; Pogoncheff et al., 2023), have significantly improved predictive models. However, while task driven models work well for responses from macaque visual cortex, they do not necessarily work as well for mouse visual cortex (Cadena et al., 2019b). Since our focus are recordings from mouse visual cortex, we fo-

cus on data-driven models, trained end-to-end on neuronal activity in the following. Early work focused on developing specialized stimulus feature representations (*cores*, Antolík et al., 2016; Ecker et al., 2018) or readout architectures (Klindt et al., 2017; Lurz et al., 2021) that map the output of the core to neuronal representations. Sinz et al. (2018) extended the core to video stimuli, adding a gated recurrent unit, and incorporating behavioral data such as pupil dilation and running speed. The inclusion of these behavioral variables allows the model to capture aspects of latent brain state and their interaction with neuron selectivity. For instance, Franke et al. (2022) showed that behavioral activity modulates stimulus selectivity in mouse visual cortex when processing colored natural scenes. Höfling et al. (2022); Vystřilová et al. (2024) further improved core architectures with factorized 3D convolutions for dynamic stimuli, achieving faster training and better performance than GRU-based models. In parallel, Wang et al. (2023a) introduced a foundational model for mouse visual cortex with a preprocessing module that adjusts for pupil position and integrates recurrent components into the core. Recently, transformer-based models (Li et al., 2023; Antoniadou et al., 2024) have shown promising results.

While these models reproduce biological phenomena and achieve state-of-the-art performance, they all train point-estimators, i.e. deterministic networks that predict a single value for each trial. The lack of a proper probabilistic model prevents them from computing log-likelihoods and limits their ability to model the stochastic distribution of neuronal activity. Wu et al. (2024) proposes a variational model for the network weights to model neurons distribution but this model only takes visual stimuli as input and does not model the latent state.

Probabilistic models focused on a latent state. Previous work has made significant progress in reducing high-dimensional neuronal recordings to smooth low-dimensional manifolds, often interpreted as latent states. However, these models ignore animal sensory experience, limiting their ability to capture contextual influences. Yu et al. (2008) introduced Gaussian Process Factor Analysis to map neural activity over time into a low-dimensional space, assuming a Gaussian distribution for neural activity given the latent variable at each time point. Jensen et al. (2021) scaled it up with a variation inference approach and Gokcen et al. (2022) extended further by incorporating time delays to model interactions between neural populations, revealing distinct latent dimensions for shared and region-specific neural dynamics. Building on this, Gokcen et al. (2023) introduced a shared latent space across sessions. However, these models assume a simple linear-Gaussian relationship between latent variables and neural activity.

To extend into nonlinear modeling, works like Sussillo et al.

(2016); Zhou & Wei (2020); Zhu et al. (2022); Schneider et al. (2023) employ variational autoencoders. The encoder learns the approximate posterior $q(z|y, a)$ for latent variables z based on neural responses y and auxiliary data a , while the decoder reconstructs neural data from z . Sussillo et al. (2016) uses a generative recurrent network to model temporal dependencies in z for neuronal spikes. Zhu et al. (2022) extended this work for calcium recordings using zero-inflated gamma distribution as a loss. In contrast, Schneider et al. (2023) trains with contrastive loss, integrating behavior or task information to produce similar embeddings for comparable neural activity. Similarly, Zhou & Wei (2020) models dependencies between task labels u , latents z , and observations x with a two-stage non-contrastive approach.

Models using sensory and neuronal input to predict other neurons’ activity. Recently appeared recurrent state space models (RSSMs) also derive latent states, for instance, Glaser et al. (2020) uses observed neural activity and exogenous factors to derive a latent state, however, their model is limited to discrete states. Zoltowski et al. (2020) is able to predict both discrete and continuous random states, however, their model is limited for the decision-making task. Apart from RSSMs, Kim et al. (2023) uses flow model, taking both task-relevant inputs and some neurons to predict responses of the other neurons but focus on auditory cortex, where both task and neuronal inputs are time series. To our knowledge, Bashiri et al. (2021) is the only work combining visual input with a latent state. It extends the core-readout framework by adding flow-modeled, stimulus-conditioned variability, including noise correlations, to the mean activity predicted by the core-readout model. However, the model of Bashiri et al. (2021) limited to static stimuli. Since its approach requires a covariance matrix between the responses of all neurons to an image, it scales quadratically with the number of neurons. This makes it computationally too expensive for temporal dependencies, since it would scale quadratically in the number of neurons and timepoints.

3. Proposed latent model

In this work we modify a well-established deterministic core-readout framework — consisting of a factorized 3D convolutional core (Vystrčilová et al., 2024) and a Gaussian readout (Lurz et al., 2021)— to a probabilistic latent state architecture (for details see Appendix C). Specifically, we add an encoder that takes a subset of neurons as input, reduces their dimensionality, and derives a latent variable. This latent state is then combined with the transformed visual input to predict the activity of other neurons from the same session. This model is equivalent to a latent variable model that predicts neuronal activity from two independent factors i) latent state and ii) the input video. In contrast to previous work (Bashiri et al., 2021), our model is video

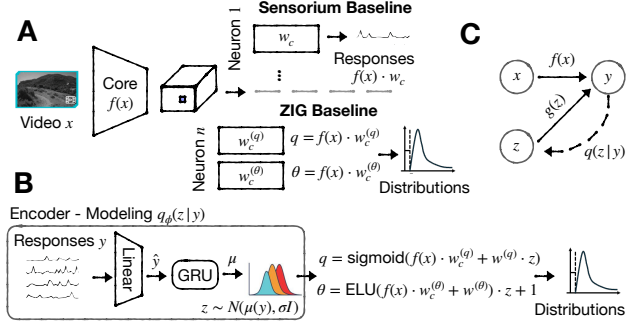


Figure 2. **A.** A 3D convolutional neural network-based core extracts features of the video-input \mathbf{x} . The readout learned the spatial position (purple dot). The deterministic Poisson baseline predicts the mean response via a per-neuron affine function from the learned feature vector \mathbf{w}^c . For the ZIG baseline, we doubled the dimension of \mathbf{w}^c to $\mathbf{w}^{(q,\theta)}$ to predict response distribution parameters q, θ of a ZIG-distribution. **B.** For the latent model, we keep the core readout $\mathbf{w}^{(q,\theta)}$ same as in the ZIG baseline and additionally add the latent variable \mathbf{z} to predict q, θ . The encoder (approximate posterior) first reduces the dimensionality of masked neuronal responses \mathbf{y} . Afterwards, a GRU computes the posterior $q(\mathbf{z}|\mathbf{y}) \sim \mathcal{N}(\mu(\mathbf{y}), \sigma\mathbf{I})$, from which we sample the latents state, when condition on the neurons. For the marginal distribution $p(\mathbf{y}|\mathbf{x})$ we sample the latents from the prior $\mathcal{N}(0, \mathbf{I})$. **C.** Directed graphical model of video, latent and response variables. The dashed line indicates the variational approximation.

based and predicts time series of neuronal response and the corresponding marginal distribution for each neuron and time point. We structured our model so that the predictions for a population of neurons can be conditioned on an arbitrary number of neurons from the same experiment. In addition, it can explicitly infer the latent state allowing us to analyze its relation to other external factors such as the behavior of the animal.

Model architecture. Our model predicts time-varying neuronal responses $\mathbf{y} \in \mathbb{R}^{N \times T}$ to a video stimulus $\mathbf{x} \in \mathbb{R}^{W \times H \times T}$, where N is the number of neurons, T the number of time points, and W and H are the frames’ width and height. The prediction also depends on a dynamic, stimulus-independent latent factor $\mathbf{z} \in \mathbb{R}^{k \times T}$ with latent dimension $k \ll N$ (Fig 2). Combining ideas from Bashiri et al. (2021) and Zhu et al. (2022), we model the distribution of neuronal responses conditioned on the stimulus and the latent factor as a Zero-Inflated-Gamma (ZIG) distribution which is a non-overlapping mixture of a uniform distribution modeling the zero-responses, and a shifted Gamma distribution modeling

the nonzero responses (Wei et al., 2019):

$$p_{\text{ZIG}}(\mathbf{y}|\mathbf{x}, \mathbf{z}; \psi) = \prod_{y_{it} \leq \rho}^{N, T} \left((1 - q_{it}(\mathbf{x}, \mathbf{z}; \psi)) \cdot \frac{1}{\rho} \right) \quad (1)$$

$$\cdot \prod_{y_{it} > \rho} \left(q_{it}(\mathbf{x}, \mathbf{z}; \psi) \cdot \text{Gamma}\left(y_{it}; \rho, \kappa_i, \theta_{it}(\mathbf{x}, \mathbf{z}; \psi)\right) \right), \quad (2)$$

where ρ is simultaneously the width of the uniform part and the shift of the Gamma distribution, κ_i the shape parameter per neuron i , q_{it} the nonzero response probability, and θ_{it} the scale parameter for each neuron at time-step t . $\text{Gamma}(\cdot; \rho, \kappa, \theta)$ is the probability density function of a Gamma distribution shifted by ρ . Our latent model predicts the distribution parameters θ and \mathbf{q} based on a given video-stimulus, the encoded latent factors and model’s parameters ψ :

$$q_{it}(\mathbf{x}, \mathbf{z}, \psi) = \text{sigmoid}\left(f_{it}^{(q)}(\mathbf{x}; \psi) + \mathbf{w}_i^{(q)} \cdot \mathbf{z}_t\right) \quad (3)$$

$$\theta_{it}(\mathbf{x}, \mathbf{z}, \psi) = \text{ELU}\left(f_{it}^{(\theta)}(\mathbf{x}; \psi) + \mathbf{w}_i^{(\theta)} \cdot \mathbf{z}_t\right) + 1. \quad (4)$$

κ_i is fitted independent of the stimulus once per neuron on the train set via moment matching to avoid ambiguity during model training. Since the expected value $\kappa \cdot \theta$ is used to predict neurons responses, allowing κ to grow uncontrolled while θ decreases proportionally could destabilize training and produces non-interpretable results.

We model $f_{it}^{(q)}$ and $f_{it}^{(\theta)}$ using a typical core-readout architecture (Fig 2A) where the core extracts features of the video-input, and the readout maps the relevant features from the core-output to the individual neurons (Turishcheva et al. (2023)). While the core has the same architecture as a model without latent state, we doubled the feature vectors of the classical Gaussian readout to predict both q and θ . We additionally tested to decode the latent variables replacing \mathbf{z}_t with smoothed latent variables $g(\mathbf{z}_t)$ in Eq. 3, 4. However, this did not improve the models’ performance (Appendix D). The stimulus-independent latent factors are modeled with a isotropic Gaussian prior across time and factors $p(\mathbf{z}) = \mathcal{N}(0, \mathbf{I})$. We model an approximate posterior (Figure 2B) as a Gaussian with the mean as function of the responses \mathbf{y} , the encoder parameters ϕ and an independent variance: $q(\mathbf{z}|\mathbf{y}; \phi) = \mathcal{N}(\mu(\mathbf{y}; \phi), \sigma^2 \mathbf{I})$.

Training We fit the model by maximizing $p_{\text{ZIG}}(\mathbf{y}|\mathbf{x})$ via its evidence lower bound (ELBO) via variational inference (Kingma & Welling, 2022; Blei et al., 2017):

$$\log p_{\text{ZIG}}(\mathbf{y}|\mathbf{x}) \geq \langle \log p(\mathbf{y}|\mathbf{z}, \mathbf{x}) \rangle_{\mathbf{z} \sim q_\phi(\mathbf{z}|\mathbf{y})} \quad (5)$$

$$+ D_{\text{KL}}[q_\phi(\mathbf{z}|\mathbf{y}) : p(\mathbf{z})], \quad (6)$$

where $\langle \cdot \rangle$ represents expected value and D_{KL} the Kullback-Leibler divergence. The likelihood term

$\langle \log p(\mathbf{y}|\mathbf{z}, \mathbf{x}) \rangle_{\mathbf{z} \sim q_\phi(\mathbf{z}|\mathbf{y})}$ of the ELBO is computed via Monte-Carlo sampling by drawing samples \mathbf{z} from the approximate posterior $q_\phi(\mathbf{z}|\mathbf{y})$. We found that 150 samples are optimal (Appendix B). Since $q_\phi(\mathbf{z}|\mathbf{y}), p(\mathbf{z})$ are Gaussians, we computed the Kullback-Leibler divergence analytically. In all of the experiments the latent model was initialized with a pretrained video-only ZIG model, unless stated otherwise.

Marginalization To compare the latent model with the baselines, which do not take neuronal activity as input, we sample the latent from the prior and marginalize \mathbf{z} via Monte-Carlo sampling to compute the response likelihoods given only the video $p(\mathbf{y}|\mathbf{x})$:

$$p(\mathbf{y}|\mathbf{x}) = \int p(\mathbf{y}|\mathbf{x}, \mathbf{z})p(\mathbf{z}) d\mathbf{z} = \frac{1}{L} \sum_l^L p(\mathbf{y}|\mathbf{x}, \mathbf{z}^{(l)}). \quad (7)$$

Appendix B indicates that the log-likelihood stabilizes and approaches a plateau after approximately 1000 samples.

4. Experiments

Dataset. We trained and evaluated our models on the data from the five mice of the SENSORIUM competition (Turishcheva et al., 2023). The SENSORIUM IDs of the mice are in Appendix F. Responses are 2-photon calcium traces from $\sim 40,000$ excitatory neurons of five mice in layers 2–5 of the primary visual cortex. They were recorded at 8 Hz while the head fixed mice viewed naturalistic gray-scale videos at 30 Hz. The signals were synchronized and upsampled to 30 Hz. During training, we used video input with shape $(W, H, T) = (64, 36, 80)$, while for evaluation we used the whole length T for each video. Behavioral variables—locomotion speed, pupil dilation and center position—were also recorded and resampled to 30 Hz.

Baseline models. We trained (1) a video-only ZIG-model (without latent) that maps video-stimulus \mathbf{x} to dynamic responses \mathbf{y} , and a (2) non-probabilistic model trained with Poisson loss (Turishcheva et al. (2023)). All models share the same hyperparameters wherever possible (Table 7). Since we aim to use correlations between latent variables and behavioral variables (Stringer et al., 2019; Bashiri et al., 2021) as external validation for the model, we excluded behavioral data during training for all models – in contrast to previous work (Sinz et al., 2018; Wang et al., 2023a).

Evaluation For each neuron i , we compute the correlation between the neuron response predictions \hat{y}_{jti} and the actual responses y_{jti} over all time points t of all video j in the evaluation data. We report the average correlation across neurons. We evaluate the model in two scenarios. In the first “video only” scenario we use the mean of the response

distribution as predictor

$$\hat{y}_{ji} = \int \mathbf{y}_i \cdot p(\mathbf{y}_i | \mathbf{z}, \mathbf{x}_j) p(\mathbf{z}) d\mathbf{z} = \langle \mathbf{y}_i \rangle_{\mathbf{y}_i \sim p(\mathbf{y}_i | \mathbf{z}, \mathbf{x}_j) p(\mathbf{z})}$$

We approximate the mean with Monte-Carlo by drawing samples $\mathbf{z}^{(l)}$ from the prior. Here, \mathbf{y}_{ij} is the predicted time series of the response of neuron i to video j .

In the second—“neuron conditioned”—scenario, we compute $\hat{y}_{ji} = \langle \mathbf{y}_i \rangle_{\mathbf{y}_i \sim p(\mathbf{y}_i | \mathbf{z}, \mathbf{x}_j) p(\mathbf{z} | \mathcal{Y}_{\mathcal{I}})}$ where \mathcal{I} is an index set that selects a subset of the population of neurons. Algorithmically, the only difference between the scenarios is how we sample \mathbf{z} .

For the ZIG based models, we use the mean of the predicted ZIG-distribution as responses prediction when computing the correlation. As we model full response distributions we also compute the log-likelihood to evaluate how well those distributions are predicted. For our latent model the latent variables \mathbf{z} are marginalized out via Monte-Carlo sampling (see Equation (7)). Per experiment details are in Appendix E

Video only evaluation: Latent model outperforms ZIG baseline We find that the Poisson baseline outperforms all other models with respect to correlation (0.195, Table 1), while the latent model outperforms all other models in terms of log-likelihood (-0.30 bits per timepoint and neuron) demonstrating the improved capability of the latent model for capturing the full response distributions. Since the neuronal responses are continuous and the Poisson distribution is for discrete values only, we cannot evaluate the log-likelihood of the Poisson model. The slightly lower correlation performance of the ZIG-models could be due the fact that the ZIG distribution is not in the exponential family which leads to a trade-off between modeling the distribution (good for likelihood) and modeling the conditional mean (good for correlation) (Lurz et al., 2023).

Table 1. Predictive performance of models. Log-likelihood is computed in Bits per Neuron and Time. Standard error of the mean (SEM) is reported across three models with different initialization.

	Poisson Baseline	Video-only ZIG	Latent ZIG
Pearson Correlation \uparrow	0.195 ± 0.003	0.183 ± 0.003	0.182 ± 0.004
Log-Likelihood \uparrow	-	-0.98 ± 0.04	-0.30 ± 0.05

Conditioning on neurons improves performance. We assessed the predictive correlation of models with (1) different latent dimensions k and (2) varying portions of responses $\mathcal{Y}_{\mathcal{I}}$ as input. Throughout, we report the correlation on a quarter of neurons population ($n \approx 2000$) per mouse, which was never used as input, i.e. where not part of the index set \mathcal{I} . Given half of the neurons responses as input (Figure 3

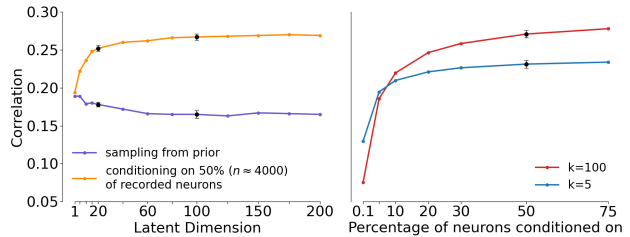


Figure 3. Left: Average correlation between predictions and ground truth responses for models with different latent dimensions. Right: Average conditioned correlation of models with a low or high dimensional latent space if different portions of neuron population are given. The error bars indicate the SEM between three models trained on different seeds. To save training costs, the standard error was not calculated at all points.

top), our latent model achieves a performance of up to 0.27 (± 0.003), a boost of 0.09 compared to the video only prediction performance of 0.18. Beyond a latent dimension of 80 we do not observe significant improvements. However, in the video only scenario, increasing the latent dimension actually decreases the correlation from the 0.18 of the latent model to 0.16. One possible reason for this could be that increasing the latent dimension enhances the latent model’s encoding capabilities, while the video-processing component remains unchanged. As a result, the model may rely more on the encoded responses in the latent variables, which might hurt the correlation if we sample from the prior.

We further explore the effect of conditioning on different portions of the neuron population on the predictive performance of a low ($k = 5$) and high ($k = 100$) model. For the low-dimensional latent model, the performance levels off when conditioned on 30% of the neuron population, reaching a correlation of about 0.23 (± 0.004). In contrast, the high-dimensional latent model keeps improving with more neurons given to the encoder, finally reaching a correlation of 0.28 (± 0.004) when 75% of neuron responses are given (Figure 3). For small portions $\mathcal{Y}_{\mathcal{I}}$ the latent model performs even worse than the video-only ZIG model. If we adapt the percentage of masked neurons during training to the percentages during evaluation (if we evaluate on 5% during evaluation, we mask 95% of neuron responses during training), the latent model performs at least as good as the video-only model for conditioning on a small subset of neurons, but it does not increase the performance for conditioning on a large portion of neurons.

Increasing latent dimension improves log-likelihood.

Because the correlation decreases with the latent dimensionality in the video-only scenario, one might expect a decline in log-likelihood performance as well, while it is actually growing with higher latent dimension (Figure 4). To analyze this apparent discrepancy, we checked how the vari-

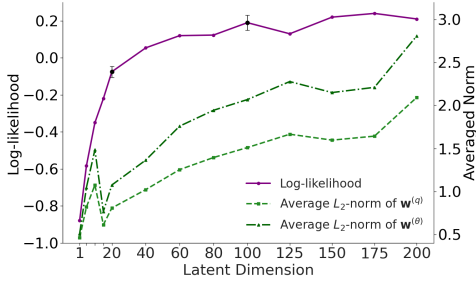


Figure 4. Comparison of log-likelihood and the average norm of the latent feature vectors $\mathbf{w}_i^{(q)}$, $\mathbf{w}_i^{(\theta)}$ across models with different latent dimensions.

ance of the latent factors affects the log-likelihood. Since the average norm of the latent feature vectors $\mathbf{w}_i^{(q,\theta)}$ increases with the latent dimension, the variance of distribution $\mathbf{w}_i \cdot \mathbf{z}_t \sim \mathcal{N}(0, \|\mathbf{w}_i\|_2^2)$ increases as well (4). Eqs. 3 and 4 show that if $\mathbf{w}_i \cdot \mathbf{z}_t$ has an increased variance, we sample the distribution parameters q, θ from a broader range. Hence, a high dimensional model is more likely to put some probability mass to more extreme response values and does not concentrate all the probability mass around the mean. Examples can be seen in Appendix G. This improves the log-likelihood $\log p(\mathbf{y}|\mathbf{x}) \approx \log(\sum_l p(\mathbf{y}|\mathbf{x}, \mathbf{z}^{(l)})) - \log(L)$, since its more likely to sample a probability density function $p(\cdot|\mathbf{x}, \mathbf{z}^{(l)})$ which has a positive value at \mathbf{y} even for extreme response values \mathbf{y} . Thus, a high dimensional model predicts more realistic response distributions by better accounting for potential outliers.

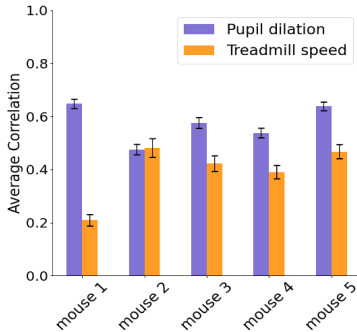


Figure 5. Canonical correlation of behavior and latent for each mouse. The CCA analysis was done with 5-fold cross-validation in an 80/20 split. The error bars indicate the standard error of the mean of cross-validation.

Latent variables strongly correlate with behavior. To test whether the latent variables sampled from our approximate posterior capture relevant internal states of the brain, we computed a canonical correlation analysis (CCA), which finds the linear combination of the latent variables $\mathbf{z}^{(1)}, \dots, \mathbf{z}^{(k)}$ with maximal correlation to a chosen behavioral variable like pupil dilation or treadmill speed. Although our model has not seen any behavioral data during training the learned latents show strong correlations with behavioral data (Figure 5). This agrees with previous works (Stringer et al., 2019; Bashiri et al., 2021; Niell &

Stryker, 2010) and suggest that our latents indeed encode meaningful brain-state related information. Analysis details can be found in Appendix H.

Feature vectors of a latent model exhibits topographic organization. Inspired by (Bashiri et al., 2021), we explore whether the latent space relates to the cortical positions of neurons in this section. The latent space model has learned two feature vectors, $\mathbf{w}_i^{(\theta)}$ and $\mathbf{w}_i^{(q)}$, for each neuron i , helping to predict parameters of the response distribution as described in Equation (3) and Equation (4). To visualize if these vectors exhibit a spatial organization on the cortical surface we computed the most relevant direction in the weight spaces and color a scatter plot of neuron location on the cortical surface by their value. The neurons depth did not affect the patterns on the xy-plane (Figure 6 row 1,2). To determine the most relevant dimensions, we performed a singular value decomposition (SVD) on the feature matrices, extracting the singular vectors $u_1, u_2, \dots \in \mathbb{R}^k$ that do explain most of the variance in the weight vectors. Subsequently, we project each weight vector onto the first three SVs via $u_j \cdot \mathbf{w}_i^{(q)}$ and $u_j \cdot \mathbf{w}_i^{(\theta)}$ for $j = 1, 2, 3$ and each neuron i . By definition of a SVD, the first singular dimensions explain most of the variance across the learned latent feature vectors. The visualization for $\mathbf{w}^{(q)}$ is in Figure 6, similar visualizations for $\mathbf{w}^{(\theta)}$ are provided in Appendix I. Interestingly, although our model was not explicitly provided with cortical position data during training, it still learned patterns that suggest a spatial organization by cortical position (Figure 6, rows 1-3). These patterns appear to be independent of the neurons’ depth in the cortex (Figure 6, rows 1 and 2). Thus, the cortical position of a neuron seems to contain highly relevant information for predicting neuron responses. Beyond the third singular dimension we did not find more spatially organized patterns.

Parameter-based latents capture information beyond spatial location. Figure 6 suggests that neighboring neurons behave the same way. This means that we can restrict the model to only use cortical position data for predict $\mathbf{w}_i^{(\theta)}$ and $\mathbf{w}_i^{(q)}$ vectors. To check this hypothesis, we trained another model where the feature vectors were explicitly determined based on cortical positions. For given coordinates p_x, p_y, p_z of neuron i in the cortex, this model computes $\mathbf{w}_i^{(q,\theta)} = h^{(q,\theta)}(p_x, p_y, p_z)$, where $h^{(q)}$ and $h^{(\theta)}$ are two simple 2-layer perceptrons. With only slight decrease in log-likelihood and correlation (Table 2) this model learned similar patterns to those observed in the model trained without cortical data (Figure 6, row 4). In addition, we trained and evaluated a third model that uses the same feature vectors, $\mathbf{w}^{(\theta)}, \mathbf{w}^{(q)}$, for all neurons only with a different scaling. This model performed worse, indicating that the feature vectors do not only change in scale but the relative contribution of each latent variable along the cortical surface. The

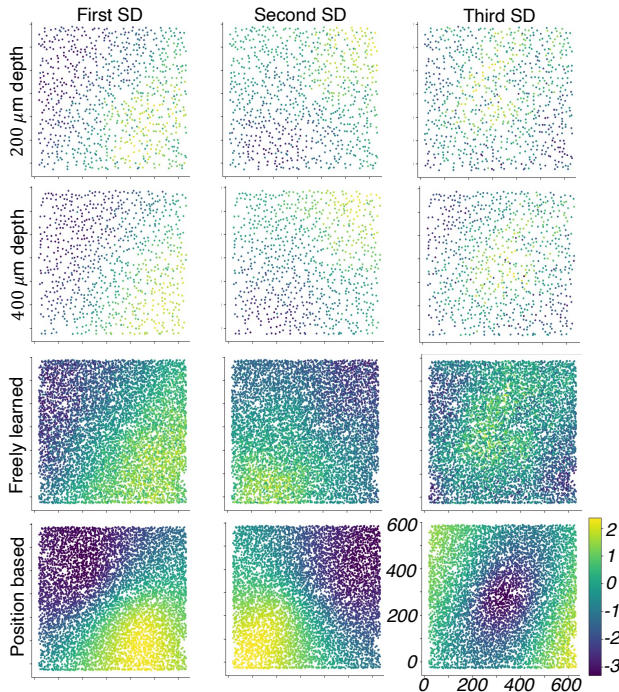


Figure 6. Color gradient maps of the latent feature vectors $\mathbf{w}_i^{(q)}$ along the first three Singular Dimensions for mouse 4. All recorded neurons are located within a $600\mu\text{m} \times 600\mu\text{m}$ square in the cortex. Their depth differs at most $200\mu\text{m}$. The first three rows display the color maps for a model with freely learned feature vectors, trained without any knowledge of cortical positions. Rows 1-2 use only neurons from a specific depth for both SVD and visualization; row 3 includes all neurons for both. Row 4 shows a model predicting latent features from cortical positions. Columns show the top three singular dimensions in descending order.

fact that both, the freely learned and position based model, yielded the same topographical organization suggests that these maps are robust and prominently contained in the data.

Position-based latent can extrapolate to unseen neurons.

The previous experiment suggests a strong topographic organization of the influence of the latent state onto the neuronal activity distribution. To test this organization further, the MLP is used to predict the weight vectors $\mathbf{w}_i^{(\theta)}$ and $\mathbf{w}_i^{(q)}$ for unseen neurons not used for training any part of the network before. In the experiment, we removed $N = 500$ neurons per mouse, trained the latent state model, latent MLP, and readout, and subsequently fine-tune feature weights and spatial position of the readout on the held out N neurons (Table 3 ‘Extrapolation’). Only the weights and spatial position of $f_{it}^{(q)}$ and $f_{it}^{(\theta)}$ are fine-tuned, while $\mathbf{w}_i^{(\theta)}$ and $\mathbf{w}_i^{(q)}$ are predicted by the previously trained MLP. We compare the performance of the fine-tuned model on those $N = 500$ neurons against a model which was trained end-to-end on

Table 2. Comparison of log-likelihood (in bits per Neuron and Time) and conditioned correlation of models with differently learned latent feature vectors $\mathbf{w}^{(\theta)}$, $\mathbf{w}^{(q)}$. The feature vectors are learned as independent model parameters (freely learned), or determined by a MLP using their cortical positions (position based) or they are the same vector with varying scales (same). All models had a latent dimension of $k = 12$

	Freely learned	Position based	Same
Log-likelihood \uparrow	-0.34	-0.69	-0.88
Conditioned Correlation \uparrow	0.24	0.22	0.18

all neurons (Table 3 ‘Original’). We find that the position-based latent model can extrapolate the mapping of latents to unseen neurons using only their cortical position with almost no drop in predictive performance.

Table 3. Correlation for 500 held-out neurons per mouse, conditioned on half of the training neurons (‘Neurons’). We compare a model which was trained on all neurons (‘Original’) against the model which has to extrapolate the mapping from the latents to those neurons (‘Extrapolation’). SEM across mice. Models for this experiment were trained from scratch.

	Neurons	Original	Extrapolation
Mouse 1	3932	0.185	0.185
Mouse 2	3954	0.255	0.245
Mouse 3	3970	0.205	0.205
Mouse 4	4101	0.215	0.210
Mouse 5	4061	0.205	0.205
Average	4003	0.213 ± 0.0005	0.210 ± 0.0004

Latents primarily reflect a stimulus-independent brain-state.

To check if the encoded latent variables actually encode information about a shared general brain state independently of the visual stimulus, we did two control experiments. For this and next experiments we used different mice, for which the responses for stimuli repeats are publicly available. In the first experiment, we compute the local contrast c_{it} for each time point t and each neuron i measured via the pixel variance in the receptive field of the neuron for the given video frame. The receptive field is determined by the maximal receptive field of the convolutional core—as determined by the kernel sizes—at the readout location of the neuron. We performed a linear regression $\text{argmin}_{W,b} \sum_{t \text{ in train}} \|W\mathbf{c}_t + \mathbf{b} - \mathbf{z}_t\|_2$ and computed the R^2 values of the actual latents \mathbf{z}_t and the predicted values $\hat{W}\mathbf{c}_t + \hat{\mathbf{b}}$ on the test set. \mathbf{z}_t is expressed in the coordinate system of the singular vectors of the weight space of the feature vectors $\mathbf{w}^{(q)}$ aligning it with the most relevant dimensions. We performed a 5 fold cross-validation on the

Table 4. (1) Contrast R^2 , standard error of mean is based on the five-fold cross-validation results (2) Conditioned Correlation, (3) Correlation for mixed repeats. (4) Correlation with sampling from the prior (video-only). For the correlations, the SEM is the average error over all neurons and videos. For each video and neuron the SEM was computed across all repeats.

	Contrast (R^2) ↓	Correlation (same repeat) ↑	Correlation (mixed repeats) ↓	Correlation (video-only) ↑
Mouse 6	0.05 ± 0.03	0.17 ± 0.02	0.12 ± 0.01	0.12 ± 0.02
Mouse 7	-0.19 ± 0.20	0.19 ± 0.02	0.16 ± 0.02	0.15 ± 0.01
Mouse 8	0.27 ± 0.01	0.20 ± 0.02	0.17 ± 0.02	0.16 ± 0.01
Mouse 9	-0.03 ± 0.04	0.24 ± 0.03	0.21 ± 0.02	0.18 ± 0.01
Mouse 10	0.01 ± 0.04	0.21 ± 0.02	0.15 ± 0.02	0.14 ± 0.01
Average	0.02 ± 0.07	0.20 ± 0.01	0.16 ± 0.01	0.15 ± 0.09

validation data to compute the average R^2 values. For 4 of the 5 mice, the video contrast does not explain the variance of the latents well. However, for one mice we get values up to 0.27 (± 0.01) indicating that the encoded latents are not fully independent from the visual-stimulus (Table 4).

In the second experiment, we use repeated stimuli to validate that the model encodes brain state-related and not visual-input related information. We split the neuronal population into two halves $\mathbf{y} = (\mathbf{y}_{\text{one_half}}, \mathbf{y}_{\text{other_half}})$, shuffled the matching of the halves across trials that presented the same stimulus, and used the shuffled pairs to predict $\mathbf{y}_{\text{one_half}}$ via $p(\mathbf{y}_{\text{one_half}}^{(i)} | \mathbf{x}, \mathbf{y}_{\text{other_half}}^{\pi(i)})$, where i and $\pi(i)$ denote the index of the original and shuffled trial. This approach ensures that $\mathbf{y}_{\text{other_half}}$ corresponds to the same video but a different brain state. If \mathbf{z} primarily captures video responses, the performance should not decline significantly. Conversely, if \mathbf{z} mostly reflects brain state, performance should drop to the level without conditioning—or worse. Table 4 shows that the correlation drops for all mice when conditioning on mixed repeats versus same-repeat responses, indicating that the latents encode a stimulus-independent brain state.

Distributional modeling helps on out-of-distribution stimuli. To test for generalization, we evaluated our model on SENSORIUM (Turishcheva et al., 2023) bonus track out-of-distribution (OOD) stimuli with different spatiotemporal statistics, such as pink noise. Point-estimate models empirically struggle on OOD tasks (Table 5 ‘Poisson’¹) when response distributions shift with stimuli. Learning per-neuron distributions improves OOD performance (‘ZIG’). The latent model, pretrained on ZIG, performs similarly when sampling from prior (‘Non-Conditioned’). Conditioning on half the neurons further boosts correlations, nearing in-domain performance (‘Conditioned’), showing that encoding neuron responses generalizes to OOD. Without pretraining, it performs poorly unless conditioned (Appendix J).

¹The Poisson baseline numbers are lower than in SENSORIUM baseline as we do not use behaviour data

Table 5. Correlations on half of neurons for out-of-distribution (OOD) stimuli, averaged across three OOD per mouse. The other half was used for conditioning. Latent model had $k = 12$.

	Poisson	ZIG	Non-Conditioned	Conditioned
Mouse 6	0.058	0.091	0.091	0.156
Mouse 7	0.097	0.128	0.128	0.174
Mouse 8	0.110	0.134	0.133	0.181
Mouse 9	0.084	0.118	0.115	0.185
Mouse 10	0.064	0.091	0.087	0.153
Average	0.08±0.009	0.11±0.008	0.11±0.007	0.17±0.009

5. Discussion

Cortical neuron activity variability arises primarily from two sources: stimulus-driven variability and internally driven variability from unobserved processes, such as behavioral tasks or brain states, which induce correlated activity across neurons. In this work we showed that adding latent factors to a video encoding model enables the prediction of a joint dynamic response distribution and captures biological variables by implicitly learning correlations between latent factors and behavior. We also showed that the influence of the latent variables onto the neuronal response is topographically organized in a robust way and that the latent variables are not primarily driven by the visual input.

Limitations and future extensions. Since it is currently challenging to quantify how much variance is explained solely by visual input (Pospisil & Bair, 2020), the latent part may encode visually related information. Our controls show that latent variables mostly seem to encode stimulus independent features. However, we cannot fully exclude the possibility that our latent state does capture stimulus dependent signals. Our model also requires more parameters per neuron compared to the video only model.

Future work. Future work could investigate reducing parameters, potentially using our promising coordinate-based MLP approach, or extend the model to the few-shot learning settings as the coordinate-based MLP generalized well. One can also change distributional assumptions in the generative model, potentially learning non-isotropic or non-Gaussian latent variables with temporal dependencies, or remove the ZIG assumption from the loss and directly train flow model to match the distributions. Alternatively, one could adapt our approach to new state-of-the-art transformer models (Turishcheva et al., 2024b). Our method should be possible to integrate with most of the models within the core-readout framework. It would also be interesting to see how probabilistic modeling influences the reproducibility of *in-silico* experiments, as it does not require behavioural variables (Ustyuzhaninov et al., 2022; Turishcheva et al., 2024a).

The robust topographic organization of the latents suggests that there could be an underlying biological meaningful.

Whether the spatially organized influence represents a biological meaningful length scale of brain state, spatially organized brain waves (Ye et al., 2023), or simply reflects the retinotopical influence of visual signal onto the neuronal activity that cannot be explained by the video model, still needs to be investigated more carefully, possibly using additional verification experiments.

Impact Statement

Our model advances the understanding of neural variability, offering insights into how the brain processes sensory information. By linking internal brain states, stimulus-driven responses, and anatomical features, it contributes to uncovering cortical computational principles. Our model relies on animal data but uses existing and publicly available datasets with general protocols, making them applicable for further research. Additionally, such models can reduce the need for animal experiments by enabling in silico exploration of neural population dynamics.

References

- Akiba, T., Sano, S., Yanase, T., Ohta, T., and Koyama, M. Optuna: A next-generation hyperparameter optimization framework. In *Proceedings of the 25th ACM SIGKDD international conference on knowledge discovery & data mining*, pp. 2623–2631, 2019.
- Antolík, J., Hofer, S. B., Bednar, J. A., and Mrsic-flogel, T. D. Model constrained by visual hierarchy improves prediction of neural responses to natural scenes. *PLoS Comput. Biol.*, pp. 1–22, 2016.
- Antoniades, A., Yu, Y., Canzano, J., Wang, W., and Smith, S. L. Neuroformer: Multimodal and multitask generative pretraining for brain data, 2024. URL <https://arxiv.org/abs/2311.00136>.
- Azabou, M., Arora, V., Ganesh, V., Mao, X., Nachimuthu, S., Mendelson, M., Richards, B., Perich, M., Lajoie, G., and Dyer, E. A unified, scalable framework for neural population decoding. In Oh, A., Naumann, T., Globerson, A., Saenko, K., Hardt, M., and Levine, S. (eds.), *Advances in Neural Information Processing Systems*, volume 36, pp. 44937–44956. Curran Associates, Inc., 2023. URL https://proceedings.neurips.cc/paper_files/paper/2023/file/8ca113d122584f12a6727341aaf58887-Paper-Conference.pdf.
- Bashiri, M., Walker, E., Lurz, K.-K., Jagadish, A., Muhammad, T., Ding, Z., Ding, Z., Tolia, A., and Sinz, F. A flow-based latent state generative model of neural population responses to natural images. In Ranzato, M., Beygelzimer, A., Dauphin, Y., Liang, P., and Vaughan, J. W. (eds.), *Advances in Neural Information Processing Systems*, volume 34, pp. 15801–15815. Curran Associates, Inc., 2021. URL https://proceedings.neurips.cc/paper_files/paper/2021/file/84a529a92de322be42dd3365afd54f91-Paper.pdf.

- Bjerke, M., Schott, L., Jensen, K. T., Battistin, C., Klindt, D. A., and Dunn, B. A. Understanding neural coding on latent manifolds by sharing features and dividing ensembles, 2023. URL <https://arxiv.org/abs/2210.03155>.
- Blei, D. M., Kucukelbir, A., and McAuliffe, J. D. Variational inference: A review for statisticians. *Journal of the American Statistical Association*, 112(518):859–877, April 2017. ISSN 1537-274X. doi: 10.1080/01621459.2017.1285773. URL <http://dx.doi.org/10.1080/01621459.2017.1285773>.
- Briggs, F., Mangun, G. R., and Usrey, W. M. Attention enhances synaptic efficacy and the signal-to-noise ratio in neural circuits. *Nature*, 499(7459):476–480, 2013.
- Cadena, S. A., Denfield, G. H., Walker, E. Y., Gatys, L. A., Tolias, A. S., Bethge, M., and Ecker, A. S. Deep convolutional models improve predictions of macaque v1 responses to natural images. *PLoS computational biology*, 15(4):e1006897, 2019a.
- Cadena, S. A., Sinz, F. H., Muhammad, T., Froudarakis, E., Cobos, E., Walker, E. Y., Reimer, J., Bethge, M., and Ecker, A. S. How well do deep neural networks trained on object recognition characterize the mouse visual system? In *NeurIPS 2019 Workshop Neuro AI*, 2019b.
- Cadiou, C. F., Hong, H., Yamins, D. L., Pinto, N., Ardila, D., Solomon, E. A., Majaj, N. J., and DiCarlo, J. J. Deep neural networks rival the representation of primate it cortex for core visual object recognition. *PLoS computational biology*, 10(12):e1003963, 2014.
- Cohen, M. R. and Maunsell, J. H. R. Attention improves performance primarily by reducing interneuronal correlations. *Nature Neuroscience*, 12(12):1594, 2009.
- Cohen, M. R. and Newsome, W. T. Context-dependent changes in functional circuitry in visual area MT. *Neuron*, 60(1):162–173, 2008.
- Ecker, A. S., Berens, P., Cotton, R. J., Subramanian, M., Denfield, G. H., Cadwell, C. R., Smirnakis, S. M., Bethge, M., and Tolias, A. S. State dependence of noise correlations in macaque primary visual cortex. *Neuron*, 82(1):235–248, 2014.
- Ecker, A. S., Sinz, F. H., Froudarakis, E., Fahey, P. G., Cadena, S. A., Walker, E. Y., Cobos, E., Reimer, J., Tolias, A. S., and Bethge, M. A rotation-equivariant convolutional neural network model of primary visual cortex. *arXiv preprint arXiv:1809.10504*, 2018.
- Franke, K., Willeke, K. F., Ponder, K., Galdamez, M., Zhou, N., Muhammad, T., Patel, S., Froudarakis, E., Reimer, J., Sinz, F. H., and Tolia, A. S. State-dependent pupil dilation rapidly shifts visual feature selectivity. *Nature*, 610(7930):128–134, 2022. doi: 10.1038/s41586-022-05270-3. URL <https://doi.org/10.1038/s41586-022-05270-3>.
- Geenjaar, E., Kim, D., Ohib, R., Duda, M., Kashyap, A., Plis, S., and Calhoun, V. Learning low-dimensional dynamics from whole-brain data improves task capture, 2023. URL <https://arxiv.org/abs/2305.14369>.
- Glaser, J., Whiteway, M., Cunningham, J. P., Paninski, L., and Linderman, S. Recurrent switching dynamical systems models for multiple interacting neural populations. *Advances in neural information processing systems*, 33:14867–14878, 2020.
- Gokcen, E., Jasper, A. I., Semedo, J. D., Zandvakili, A., Kohn, A., Machens, C. K., and Yu, B. M. Disentangling the flow of signals between populations of neurons. *Nature Computational Science*, 2(8):512–525, August 2022.
- Gokcen, E., Jasper, A., Xu, A., Kohn, A., Machens, C. K., and Yu, B. M. Uncovering motifs of concurrent signaling across multiple neuronal populations. In Oh, A., Naumann, T., Globerson, A., Saenko, K., Hardt, M., and Levine, S. (eds.), *Advances in Neural Information Processing Systems*, volume 36, pp. 34711–34722. Curran Associates, Inc., 2023. URL https://proceedings.neurips.cc/paper_files/paper/2023/file/6cf7a37e761f55b642cf0939b4c64bb8-Paper-Conference.pdf.
- Haefner, R. M., Berkes, P., and Fiser, J. Perceptual decision-making as probabilistic inference by neural sampling. *Neuron*, 90(3):649–660, 2016.
- Höfling, L., Szatko, K. P., Behrens, C., Qiu, Y., Klindt, D. A., Jessen, Z., Schwartz, G. W., Bethge, M., Berens, P., Franke, K., Ecker, A. S., and Euler, T. A chromatic feature detector in the retina signals visual context changes. *bioRxiv*, 2022. doi: 10.1101/2022.11.30.518492. URL <https://www.biorxiv.org/content/early/2022/12/01/2022.11.30.518492>.
- Jensen, K., Kao, T.-C., Stone, J., and Hennequin, G. Scalable bayesian gpfa with automatic relevance determination and discrete noise models. In Ranzato, M., Beygelzimer, A., Dauphin, Y., Liang, P., and Vaughan, J. W. (eds.), *Advances in Neural Information Processing Systems*, volume 34, pp. 10613–10626. Curran Associates, Inc., 2021. URL https://proceedings.neurips.cc/paper_files/paper/2021/file/58238e9ae2dd305d79c2ebc8c1883422-Paper.pdf.

- Kim, T., Luo, T., Can, T., Krishnamurthy, K., Pillow, J., and Brody, C. Flow-field inference from neural data using deep recurrent networks. *bioRxiv*, 2023. doi: 10.1101/2023.11.14.567136. URL <https://doi.org/10.1101/2023.11.14.567136>. PMID: 38014290; PMCID: PMC10680687.
- Kingma, D. P. and Welling, M. Auto-encoding variational bayes, 2022. URL <https://arxiv.org/abs/1312.6114>.
- Klindt, D. A., Ecker, A. S., Euler, T., and Bethge, M. Neural system identification for large populations separating "what" and "where". In *Advances in Neural Information Processing Systems (NeurIPS)*. Curran Associates, Inc., November 2017.
- Li, B. M., Cornacchia, I. M., Rochefort, N. L., and Onken, A. V1t: large-scale mouse v1 response prediction using a vision transformer. *arXiv preprint arXiv:2302.03023*, 2023.
- Lurz, K.-K., Bashiri, M., Willeke, K., Jagadish, A., Wang, E., Walker, E. Y., Cadena, S. A., Muhammad, T., Cobos, E., Tolias, A. S., Ecker, A. S., and Sinz, F. H. Generalization in data-driven models of primary visual cortex. *International Conference on Learning Representations (ICLR)*, 2021. URL <https://openreview.net/>.
- Lurz, K.-K., Bashiri, M., Walker, E. Y., and Sinz, F. H. Bayesian oracle for bounding information gain in neural encoding models. In *The Eleventh International Conference on Learning Representations*, 2023. URL <https://openreview.net/forum?id=iYC5hOMqUg>.
- Mitchell, J. F., Sundberg, K. A., and Reynolds, J. H. Spatial attention decorrelates intrinsic activity fluctuations in macaque area V4. *Neuron*, 63(6):879–888, 2009.
- Niell, C. M. and Stryker, M. P. Modulation of visual responses by behavioral state in mouse visual cortex. *Neuron*, 65(4):472–479, 2010.
- Pogoncheff, G., Granley, J., and Beyeler, M. Explaining v1 properties with a biologically constrained deep learning architecture. *Advances in Neural Information Processing Systems*, 36:13908–13930, 2023.
- Pospisl, D. and Bair, W. The unbiased estimation of the fraction of variance explained by a model [publisher, 2020].
- Reimer, J., Froudarakis, E., Cadwell, C. R., Yatsenko, D., Denfield, G. H., and Tolias, A. S. Pupil fluctuations track fast switching of cortical states during quiet wakefulness. *Neuron*, 84(2):355–362, 2014.
- Schneider, S., Lee, J. H., and Mathis, M. W. Learnable latent embeddings for joint behavioural and neural analysis. *Nature*, 617(7960):360–368, May 2023.
- Seeliger, K., Ambrogioni, L., Güçlütürk, Y., van den Bulk, L., Güçlü, U., and van Gerven, M. End-to-end neural system identification with neural information flow. *PLoS Comput Biol*, 17(2):e1008558, Feb 2021. doi: 10.1371/journal.pcbi.1008558.
- Shadlen, M. N. and Newsome, W. T. The variable discharge of cortical neurons: implications for connectivity, computation, and information coding. *Journal of Neuroscience*, 18(10):3870–3896, 1998.
- Sinz, F., Ecker, A. S., Fahey, P., Walker, E., Cobos, E., Froudarakis, E., Yatsenko, D., Pitkow, Z., Reimer, J., and Tolias, A. Stimulus domain transfer in recurrent models for large scale cortical population prediction on video. In Bengio, S., Wallach, H., Larochelle, H., Grauman, K., Cesa-Bianchi, N., and Garnett, R. (eds.), *Advances in Neural Information Processing Systems*, volume 31. Curran Associates, Inc., 2018. URL https://proceedings.neurips.cc/paper_files/paper/2018/file/9d684c589d67031a627ad33d59db65e5-Paper.pdf.
- Stringer, C., Pachitariu, M., Steinmetz, N., Reddy, C. B., Carandini, M., and Harris, K. D. Spontaneous behaviors drive multidimensional, brainwide activity. *Science*, 364(6437):255, 2019. doi: 10.1126/science.aav7893.
- Sussillo, D., Jozefowicz, R., Abbott, L. F., and Pandarinath, C. Lfads - latent factor analysis via dynamical systems, 2016. URL <https://arxiv.org/abs/1608.06315>.
- Tolhurst, D. J., Movshon, J. A., and Dean, A. F. The statistical reliability of signals in single neurons in cat and monkey visual cortex. *Vision Research*, 23(8):775–785, 1983.
- Tomko, G. J. and Crapper, D. R. Neuronal variability: non-stationary responses to identical visual stimuli. *Brain Research*, 79(3):405–418, 1974.
- Turishcheva, P., Fahey, P. G., Hansel, L., Froebe, R., Ponder, K., Vystrčilová, M., Willeke, K. F., Bashiri, M., Wang, E., Ding, Z., Tolias, A. S., Sinz, F. H., and Ecker, A. S. The dynamic sensorium competition for predicting large-scale mouse visual cortex activity from videos. *arXiv*, preprint, 2023. doi: 10.48550/arXiv.2305.19654. URL <https://doi.org/10.48550/arXiv.2305.19654>.
- Turishcheva, P., Burg, M., Sinz, F. H., and Ecker, A. Reproducibility of predictive networks for mouse visual cortex. *arXiv preprint arXiv:2406.12625*, 2024a.
- Turishcheva, P., Fahey, P. G., Vystrčilová, M., Hansel, L., Froebe, R., Ponder, K., Qiu, Y., Willeke, K. F., Bashiri,

- M., Baikulov, R., et al. Retrospective for the dynamic sensorium competition for predicting large-scale mouse primary visual cortex activity from videos. *ArXiv*, pp. arXiv-2407, 2024b.
- Ustyuzhaninov, I., Burg, M. F., Cadena, S. A., Fu, J., Muhammad, T., Ponder, K., Froudarakis, E., Ding, Z., Bethge, M., Tolias, A. S., et al. Digital twin reveals combinatorial code of non-linear computations in the mouse primary visual cortex. *bioRxiv*, pp. 2022-02, 2022.
- Vystrčilová, M., Sridhar, S., Burg, M. F., Gollisch, T., and Ecker, A. S. Convolutional neural network models of the primate retina reveal adaptation to natural stimulus statistics. *bioRxiv*, 2024. doi: 10.1101/2024.03.06.583740. URL <https://www.biorxiv.org/content/early/2024/03/09/2024.03.06.583740>.
- Wang, E. Y., Fahey, P. G., Ding, Z., Papadopoulos, S., Ponder, K., Weis, M. A., Chang, A., Muhammad, T., Patel, S., Ding, Z., Tran, D., Fu, J., Schneider-Mizell, C. M., Reid, R. C., Collman, F., da Costa, N. M., Franke, K., Ecker, A. S., Reimer, J., Pitkow, X., Sinz, F. H., and Tolias, A. S. Foundation model of neural activity predicts response to new stimulus types and anatomy. *bioRxiv*, pp. 2023.03.21.533548, March 2023a. doi: 10.1101/2023.03.21.533548. URL <https://doi.org/10.1101/2023.03.21.533548>.
- Wang, Y., Wu, Z., Li, C., and Wu, A. Extraction and recovery of spatio-temporal structure in latent dynamics alignment with diffusion models. In Oh, A., Naumann, T., Globerson, A., Saenko, K., Hardt, M., and Levine, S. (eds.), *Advances in Neural Information Processing Systems*, volume 36, pp. 38988–39005. Curran Associates, Inc., 2023b. URL https://proceedings.neurips.cc/paper_files/paper/2023/file/7abbc05a5d55157ede410bb718e32d7-Paper-Conference.pdf.
- Wei, X.-X., Zhou, D., Grosmark, A., Ajabi, Z., Sparks, F., Zhou, P., Brandon, M., Losonczy, A., and Paninski, L. A zero-inflated gamma model for post-deconvolved calcium imaging traces. May 2019. doi: 10.1101/637652. URL <http://dx.doi.org/10.1101/637652>.
- Wu, N., Valera, I., Sinz, F., Ecker, A., Euler, T., and Qiu, Y. Probabilistic neural transfer function estimation with bayesian system identification. *Plos Computational Biology*, 20(7):e1012354, 2024.
- Yamins, D. L., Hong, H., Cadieu, C. F., Solomon, E. A., Seibert, D., and DiCarlo, J. J. Performance-optimized hierarchical models predict neural responses in higher visual cortex. *Proceedings of the national academy of sciences*, 111(23):8619–8624, 2014.
- Ye, Z., Bull, M. S., Li, A., Birman, D., Daigle, T. L., Tasic, B., Zeng, H., and Steinmetz, N. A. Brain-wide topographic coordination of traveling spiral waves. *bioRxiv*, pp. 2023.12.07.570517, December 2023.
- Yu, B. M., Cunningham, J. P., Santhanam, G., Ryu, S., Shenoy, K. V., and Sahani, M. Gaussian-process factor analysis for low-dimensional single-trial analysis of neural population activity. *Advances in neural information processing systems*, 21, 2008.
- Yu, B. M., Cunningham, J. P., Santhanam, G., Ryu, S. I., Shenoy, K. V., and Sahani, M. Gaussian-process factor analysis for low-dimensional single-trial analysis of neural population activity. *Journal of Neurophysiology*, 102(1):614–635, 2009. doi: 10.1152/jn.90941.2008. Epub 2009 Apr 8; Erratum in: *Journal of Neurophysiology*. 2009 Sep;102(3):2008.
- Zhou, D. and Wei, X.-X. Learning identifiable and interpretable latent models of high-dimensional neural activity using pi-vae. In Larochelle, H., Ranzato, M., Hadsell, R., Balcan, M., and Lin, H. (eds.), *Advances in Neural Information Processing Systems*, volume 33, pp. 7234–7247. Curran Associates, Inc., 2020. URL https://proceedings.neurips.cc/paper_files/paper/2020/file/510f2318f324cf07fce24c3a4b89c771-Paper.pdf.
- Zhu, F., Grier, H. A., Tandon, R., Cai, C., Agarwal, A., Giovannucci, A., Kaufman, M. T., and Pandarinath, C. A deep learning framework for inference of single-trial neural population dynamics from calcium imaging with subframe temporal resolution. *Nature neuroscience*, 25(12):1724–1734, 2022.
- Zoltowski, D., Pillow, J., and Linderman, S. A general recurrent state space framework for modeling neural dynamics during decision-making. In *International Conference on Machine Learning*, pp. 11680–11691. PMLR, 2020.

A. Related Works Overview

An overview of related work, which either predicts neuron responses for given natural stimuli, uses latent representations for encoding neuron responses or takes behavior of the animal into account, is summarized in Appendix A.

B. Monte-Carlo Approximations

We have to approximate expectation values via Monte-Carlo sample two times in our model setup. First, during training we have to calculate the likelihood $\langle \log p(\mathbf{y}|\mathbf{z}, \mathbf{x}) \rangle_{\mathbf{z} \sim q_\phi(\mathbf{z}|\mathbf{y})}$ in the ELBO via Monte-Carlo sampling (Equation (7)). Second, during evaluation we draw samples from the prior distribution $\mathcal{N}(0, \mathbf{I}_k)$, where k is the latent dimension, for calculating the log-likelihood $\log p(\mathbf{y}|\mathbf{x})$ as described in Equation (6).

The ELBO was approximated with up to 150 samples. More samples yield memory issues during training on a single A100 GPU. We observed the log-likelihood performance during inference to increase with the sample size during training as the ELBO is approximated more accurate (Figure 7). For the Monte-Carlo approximation of the marginalized log-likelihood during inference we tested different samples sizes ranging up to 5000. It was not possible to test more than 5000 samples, because at that point we ran into memory issue on a single H100 GPU. However, Figure 8 indicates that the log-likelihood stabilizes and approaches a plateau after approximately 1000 samples. We thus resorted to drawing 1000 samples to approximate the marginalized log-likelihood. The correlation performance of the latent model was not strongly influenced by the sample sizes.

C. Model Architecture and Hyperparameters Setting

The video processing part consists of a factorized 3D-CNN block followed by a Gaussian readout ((Höfling et al., 2022)). Each convolutional layer consists of a factorized 3D convolution across spatial and temporal dimension followed by a batch normalization layer and an ELU activation function. We use a variational autoencoding approach for the latent representations. A dropout layer is applied to the neuron responses before they are fed into the encoder. This prevents the model from learning correlations between specific neurons thereby encouraging the learning of global latent representations. The encoder applies a linear layer reducing the dimensionality of neuron responses $N \approx 8,000$ (N ranging from 7800 to 8200 depending on the mouse as part of the SENSORIUM dataset (Turishcheva et al., 2024a)) to $n \ll N$. For each time step the same linear layer is applied independently. The linear layer is followed by a layer normalization and an ELU activation function. An individual linear layer was trained for each mouse. The output

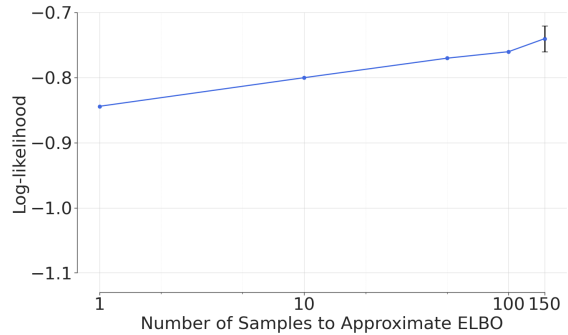


Figure 7. Log-likelihood (measured in bits per neuron and time) of models trained with different sample sizes to approximate the ELBO during training. The error bar indicates the standard error of the mean of the log-likelihood for models initialized and trained on 3 different seeds. Due to the computational cost of training a model, the standard error was calculated only at a single point.

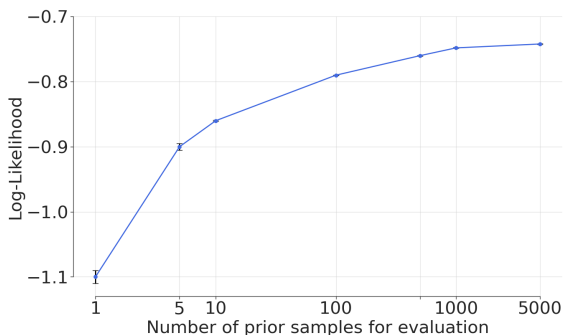


Figure 8. Log-likelihood (measured in bits per neuron and time) for different sample sizes L of the prior during evaluation. Error bars indicate the standard error of the mean for sampling from different seeds.

is processed by a one-layer recurrent neural network with gated recurrent units producing the means $\mu(\mathbf{y}; \phi)$ of the approximate posterior $q(\mathbf{z}|\mathbf{y}; \phi) = \mathcal{N}(\mu(\mathbf{y}; \psi), \sigma^2 \mathbf{I})$. σ is a learnable model parameter of the encoder. \mathbf{z} is combined with the outputs from the video encoding part computing the parameters for the probability $\log p(\mathbf{y}|\mathbf{z}, \mathbf{x})$ as in Equation (3) and Equation (4). For a graphical illustration see Figure 2. We searched over various hyperparameters (Table 7) using Optuna (Akiba et al., 2019).

Table 7. Hyperparameter Configuration

General	
Learning rate	0.005
Core	
Number Layers	3
Temporal Kernel Size first Layer	11
Spatial Kernel Size first Layer	(11,11)
Spatial Kernel Size other Layer	(5,5)
Spatial Kernel Size other Layer	(5,5)
Channels per Layer	(32,64,128)
Encoder	
Number Layers	1
Dropout probability	50%
Output Dim Linear Layer	42
Output Dim GRU	12

D. Optimizing Encoder Architecture

To ensure optimal encoding of the neuron responses we tested a 3D factorized CNN and a GRU architecture. We further tested different layer sizes ranging from 1-5. We found that a one-layer GRU encoder performs best in terms of correlation and log-likelihood.

Further, we tried to add a “smoother” g to further smooth the latents in time. Compared to the model reported above, \mathbf{z}_t is replaced by $g(\mathbf{z}_t)$ in Equation (3) and Equation (4). We tested how a model with a CNN-smoother or GRU-smoother model performed compared to a model without a smoother. As Tab. 8 indicates, replacing the GRU with a CNN does not make a significant difference. However, the model without smoother had the best performance in log-likelihood and conditioned correlation (Tab. 8).

Table 8. The columns present the performance of models with a 12-dimensional latent space, each trained using either a GRU smoother, a CNN smoother, or no smoother.

	GRU Smoother	CNN Smoother	No Smoother
Log-likelihood \uparrow	-0.74	-0.77	-0.30
Conditioned Correlation \uparrow	0.23	0.22	0.24

E. Experiment Details

Depending on the analysis setup, we adjusted the model architecture and training configuration as needed. For ex-

periments examining cortical patterns revealed by the latent model, we ensured that no positional data was provided. Although the Gaussian readout allows neuron positions to be used for spatial predictions in the video feature map, we disabled this option for these experiments (Table 9, ‘Positional Data’ column). Additionally, we found that initializing the video-processing weights of our latent model with those from a pre-trained video-only ZIG model improved predictive performance (Table 10). Therefore, we applied pretrained weights for the video component whenever the experiment setup allowed (Table 9, ‘Pretrained Video-Part’ column). Since we tested different latent dimensions, we specify the latent dimensions used for each experiment (Table 9, ‘Latent Dimension’ column). Lastly, we report the number of neurons used during evaluation (Table 9, ‘Evaluation Neurons’ column). If the same number of neurons was used for evaluation across experiments, the selected neurons remained consistent. For instance, if one-quarter of the neurons were evaluated, the same subset was used in all experiments. For a exact number of neurons per mouse see Table 11.

Table 10. Comparison of a latent model with latent dimension $k = 12$, initialized using weights from a pre-trained video-only ZIG model, against a latent model trained from scratch. We evaluate performance based on log-likelihood and correlation, considering both Conditioned Correlation (conditioning on half of the neurons) and Prior Correlation (sampling from the prior). Evaluation is conducted on half of the neuron population.

	Pre-trained	Scratch
Log-likelihood \uparrow	-0.30	-0.36
Conditioned Correlation \uparrow	0.24	0.23
Prior Correlation \uparrow	0.18	0.10

F. Mice IDs

For reproducibility, we list the Sensorium ID’s of the mice, which were used for training and evaluation in our experiments, in Table 11. In the main part, they were referred as mice 1-10. Further, Table 11 shows the exact number of recorded neurons per mice.

Table 11. Mice 1-10 of the main text with corresponding SENSORIUM IDs ('IDs'). Total numbers of recorded neurons per mouse are tracked ('Neurons').

	Neurons	ID
Mouse 1	7863	29515-10-12
Mouse 2	7908	29623-4-9
Mouse 3	7939	29712-5-9
Mouse 4	8202	29647-19-8
Mouse 5	8122	29755-2-8
Mouse 6	7440	29156-11-10
Mouse 7	7928	29228-2-10
Mouse 8	8285	29234-6-9
Mouse 9	7671	29513-3-5
Mouse 10	7495	29514-2-9

G. Heat Maps of Response Distributions

As reported in the main paper, a high dimensional latent state yields a higher log-likelihood. We explained this effect by a better "coverage" of the response space with probability mass. Here, we visualize this effect. One can see, that a high dimensional latent model is more likely to put some probability mass to a broader range of response values and does not concentrate all the probability mass around the mean (Figure 9). Thus, extreme response values, as in column 3 of Figure 9, are covered with a non-zero probability. A low-dimensional model predicts them with almost zero probability (parts of the response traces are in the gray areas of the heatmap).

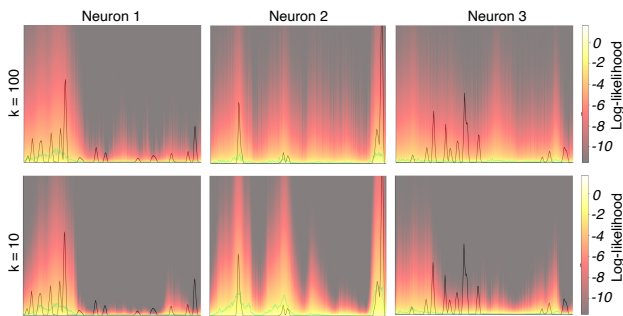


Figure 9. Neuron response traces and model predictions for one video recording. The black line represents the actual response of each neuron over time, while the cyan line represents the model's predicted response, which is the mean of the predicted ZIG distribution. For each time point, the predicted response ZIG-distribution is visualized as a heatmap along the y-axis. The top row displays predictions from a model with a latent dimension of $k = 100$, while the bottom row shows predictions from a model with a latent dimension of $k = 10$.

H. Behavior Analysis

For the pupil dilation and the treadmill speed of each mouse we performed one CCA analysis each. The CCA analysis was done with 5-fold cross validation. We split the recording time with a 80/20 ratio and fit the CCA weights on the train split. The correlations were computed between the CCA combination $\sum_i w_i^{(cca)} \mathbf{z}^{(i)}$ and the behavioural variable (pupil dilation or treadmill speed) on the test split. $w_i^{(cca)}$ are the CCA weights and $\mathbf{z}^{(1)}, \dots, \mathbf{z}^{(k)} \in \mathbb{R}^T$ are the latent variables. For each mouse, we computed the average correlation across the cross-validation. Table 12 shows the average of those correlation values across all mice. For two selected videos and mice we plotted their normalized pupil dilation and treadmill speed against the corresponding normalized CCA combination of the latent over whole videos time, which correspond to ~ 300 time points (Figure 10).

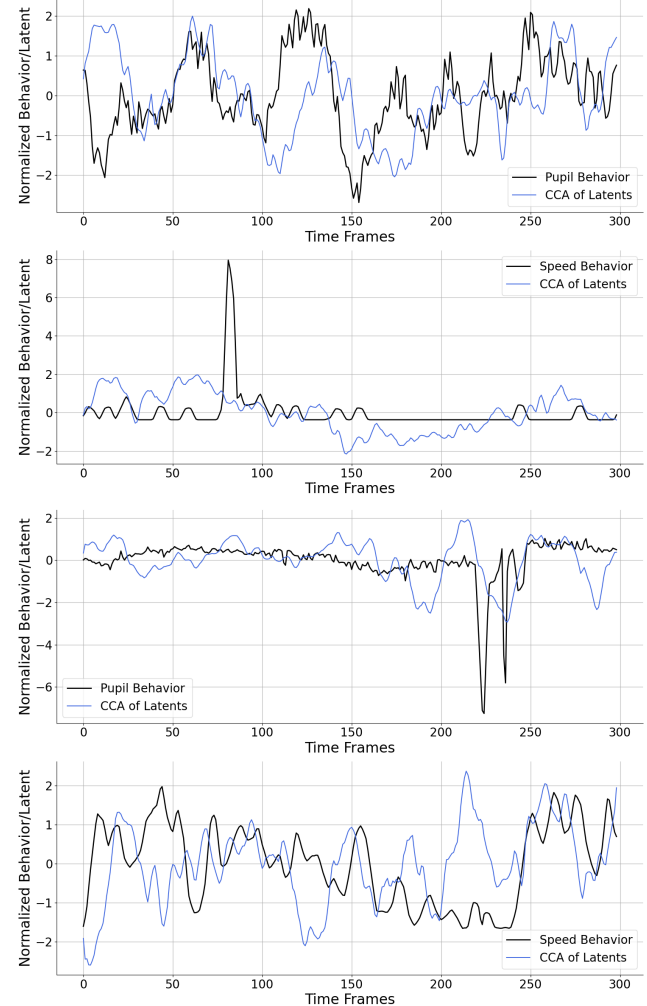


Figure 10. Normalized behavior and CCA combination of latent factors during two selected videos

Table 12. Average canonical correlation for behavior and latent with standard error of mean across all five mice

	Latent Model
Pupil Dilation	0.57 ± 0.026
Treadmill Speed	0.40 ± 0.044

I. Additional Brain Maps

In Figure 6, we showed only the first three singular dimensions of the latent feature matrix $\mathbf{w}^{(q)}$. In rows 1 and 2 of Figure 11, we compare those same three dimensions for both $\mathbf{w}^{(\theta)}$ and $\mathbf{w}^{(q)}$. They exhibit largely the same spatial patterns, aside from sign flips in columns 1 and 3. Beyond the first three dimensions, we did not observe any notable structure: Row 2-4 of Figure 11 displays singular dimensions one through nine for $\mathbf{w}^{(\theta)}$. Beyond the fourth singular dimension they do not appear to align with cortical neuron positions and seem randomly distributed across the xy-plane.

J. Latent model performance on out of distribution data

 Table 13. Latent model without ZIG pretraining, $k = 200$

	Non-Conditioned	Conditioned
Mouse 6	0.016	0.170
Mouse 7	0.029	0.196
Mouse 8	0.022	0.211
Mouse 9	0.026	0.209
Mouse 10	0.015	0.184

 Table 14. Latent model with ZIG pretraining, $k = 150$

	Non-Conditioned	Conditioned
Mouse 6	0.086	0.172
Mouse 7	0.121	0.192
Mouse 8	0.125	0.206
Mouse 9	0.107	0.207
Mouse 10	0.082	0.179

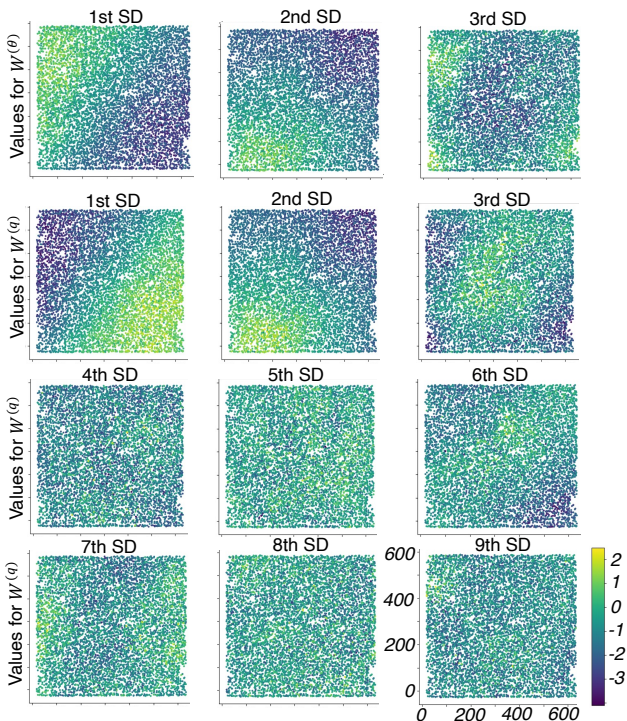


Figure 11. Row 2-4: Color gradient maps of the latent feature vectors $\mathbf{w}_i^{(q)}$ along the first nine Singular Dimensions (SD) for mouse 4. Row 1: The color gradient maps of the first three singular dimensions of the latent feature vectors $\mathbf{w}_i^{(\theta)}$ are plotted. All recorded neurons are located within a $600\mu\text{m} \times 600\mu\text{m}$ square in the cortex. Their depth differs at most $200\mu\text{m}$. The model was trained without any knowledge of cortical positions and freely learnable feature vectors.

Table 6. Summary of Reviewed Literature: **Column 2** categorizes, if the recorded neural activities are dynamic or static, and its role as input/output of the model. **Column 3** details the type of stimulus components. **Column 4** indicates if the used model has a latent space and if a distribution is computable for the latent (probabilistic). **Column 5** describes the involvement and role of behavioral data. **Column 6** lists the datasets, including subject types, data collection methods, tasks performed during recordings, and neuron sample sizes.

References	Neural activity	Stimulus	Learned latent	Behavior	Datasets
Schneider et al. (2023)	Dynamic Input	No	Yes, probabilistic	Input	Rats, Mice, Monkey 2p and electro-physiology 10-1000 Neurons
Wang et al. (2023a) Turishcheva et al. (2023) Sinz et al. (2018)	Dynamic Output	Video	No	Input	Mice, 2p, passive ~ 140,000 Neurons ~ 40,000 Neurons
Kim et al. (2023)	Dynamic In/Output	Audio	Yes, probabilistic	No	Synthetic and Rats, audio decision-making 67 Neurons
Antoniades et al. (2024) Azabou et al. (2023)	Dynamic Output	Video No	Yes, not probabilistic	Output	Mice, 2p, passive 386 Neurons Monkey 27,373 Neurons
Gokcen et al. (2022) Sussillo et al. (2016)	Dynamic Input	No	Yes, probabilistic	No	Macaque V1-3 120 Neurons Synthetic 30 Neurons
Zhou & Wei (2020) Wang et al. (2023b) Bjerke et al. (2023) Jensen et al. (2021)	Dynamic In/Output	No	Yes, probabilistic	Task Input No No	Monkey, reaching-task Rat, running 192,120 Neurons Monkey, Rat task 200 x 200 Neurons Mouse,Rats 26 and 149 Neurons Macaque, reaching-task 200 Neurons
Geenjaar et al. (2023)	Dynamic In/Output	No	Yes not, probabilistic	No	fMRI
Seeliger et al. (2021)	Dynamic Output	Video	No	No	fMRI
Bashiri et al. (2021)	Static Output	Image	Yes, probabilistic	Output	Mouse V1/LM, 2p,passive ~ 4,000 Neurons

Table 9. An overview of the details of each experiment conducted in the main text. In the row for Table 1 we only refer to the latent model.

	Positional Data	Pretrained Video-Part	Latent Dimension k	Evaluation Neurons (per mouse)
Table 1	True	True	12	All
Table 2	False	True	12	Half
Table 3	False	False	12	500
Table 4	True	True	12	Half
Table 5	True	True	12	Half
Figure 3	True	True	1-200	Quarter
Figure 4	True	True	1-200	Quarter
Figure 5	True	True	12	-
Figure 6	False	True	12	All